Intramolecular Electron-Loss Contributions to Cusp Shapes and Yields for ~1 MeV/Nucleon Bare H and He on Hydrocarbon Gases

G. Bissinger and R. Mehta[a]

East Carolina University Accelerator Laboratory, East Carolina University, Greenville, North Carolina 27858

(Received 5 August 1991)

Zero-degree $d\sigma/dE$ and $d^2\sigma/dE\,d\Omega$ cusp-shape and yield variations indicate substantial electron-loss-to-continuum (ELC) contributions in the electron-capture-to-continuum (ECC) spectra obtained with bare H and He ~1 MeV/nucleon projectiles on hydrocarbon molecules. An *intramolecular* geometrical outscattering model of secondary collisions has been developed to calculate the ELC fraction of the cusp f_{ELC}, extract the separate ECC and ELC contributions from measured projectile velocity frame cusp contours, and predict a nominal Z_p^3 dependence for ELC yields in agreement with experiments in our velocity range.

PACS numbers: 34.50.Gb, 79.20.Hx, 79.20.Nc

The question of a "standard" continuum electron spectrum shape for those unbound electrons detected at zero degrees with velocities matched to the projectile's, i.e., $v_e \cong v_p$ (commonly called the cusp), is a vexing one even for bare projectiles on atomic targets [1–4], where both the identity of the target atom and the (sub)shell origin of the continuum electron affect the cusp shape [5]. The matter of a standard cusp shape is further complicated for solid targets because these introduce multiple charge-changing processes producing both electron-loss-to-continuum (ELC) and electron-capture-to-continuum (ECC) electrons [collectively combined under the rubric of electron-transfer-to-continuum (ETC) processes] from a manifold of initial states including bound states. The complexity increases even more when uncertainties in average charge and/or excitation states of the projectile inside the solid, along with the subsequent elastic and inelastic continuum electron interactions with the solid [6] are included.

Working with small molecular gas targets, on the other hand, does not necessarily remove any of the complications attendant to the use of solid targets, *except to limit the number of secondary collisions.* In the velocity range of our H^+ and He^{++} projectiles (~5–11 a.u.) limiting the choice of molecules to hydrocarbons provides substantial additional reductions in target-atom–shell-origin effects because the electron-capture-to-bound state (ECB) and ECC total cross sections (i) are > 97% from the C atoms; (ii) are dominated ($\gtrsim$75%) by C K-shell contributions; and (iii) have minor valence electron contributions from molecules whose $2s$ and $2p$ orbital populations and binding energy variations are relatively small [7–9]. In terms of the electron-capture cross sections these hydrocarbon molecules look like a string of C atoms. On the other hand, the loss cross sections for a H atom are $\sim\frac{1}{7}$ those for C in our velocity range so that even in CH_4 there is a substantial probability of ELC from an H atom subsequent to an ECB event.

In a prior work, we examined ECB total cross-section additivity failure for 18 different C-, O-, F-, and S-bearing molecules with H^+ and He^+ projectiles over a similar velocity range [9]. An *intramolecular* geometric outscattering (IMGO) model incorporating secondary-electron-loss collisions was developed for these measurements to provide a modified additivity equation for the capture cross sections σ_{10}, e.g., for hydrocarbons

$$\sigma_{10}(C_mH_n) = T_B(C;mn)m\sigma_{10}(C) + T_B(H;mn)n\sigma_{10}(H),$$

and to extract "atomic" C, O, F, and S σ_{10} values. This equation assumes that the electron-capture cross section is the same from each C or H; the departure from strict atomic cross-section additivity arises from *postcapture* interactions, subsumed into the transmission fraction T_B. T_B for each atomic species was defined as the fraction of ECB events that traversed the residue of the molecule without a subsequent ELC interaction [10]. By incorporating relevant atomic electron-loss cross sections σ_{01} for each atom, along with the associated interatomic distance d_{ij}, $T_B = 1 - P_B$ was calculated from an average-over-all-donor-atoms-of-a-specific-atomic-species probability for electron loss $P_B = 0.5\sum_{i,j}[1 - d_{ij}/(d_{ij}^2 + a\sigma_{01}/\pi)^{1/2}]$, with fit parameter $a \sim 3$ for all data. For example, P_B values for 0.8–3.0 MeV H^+ ranged from ~0.09 to ~0.03 for CH_4 and ~0.24 to ~0.1 for C_4H_8 [9]. The production of ELC electrons implicit in the IMGO model for ECB perforce contribute to the zero-degree cusp.

To apply the IMGO model to the ETC cusp we make the following cardinal assumptions: (i) only one additional *post* ECB charge-changing collision is allowed; (ii) all ELC electrons from (i) are detected along with ECC electrons [11], with probability P_B ($= 1 - T_B$) so that the cross section for intramolecular ELC with bare incident projectiles is $\sigma_{\mathrm{ELC}} = \sigma_{\mathrm{ECB}}(1 - T_B)$; and (iii) the ETC electrons undergo subsequent intramolecular elastic and inelastic electron scattering similarly parametrized by the total electron scattering cross section σ_{tot} [8] and included via the transmission fraction T_c. These assumptions allow us to draw the schema in Fig. 1 for the IMGO model incorporating the primary ECB and ECC and secondary ELC electron transfer processes and their respective subsequent intramolecular interactions in a

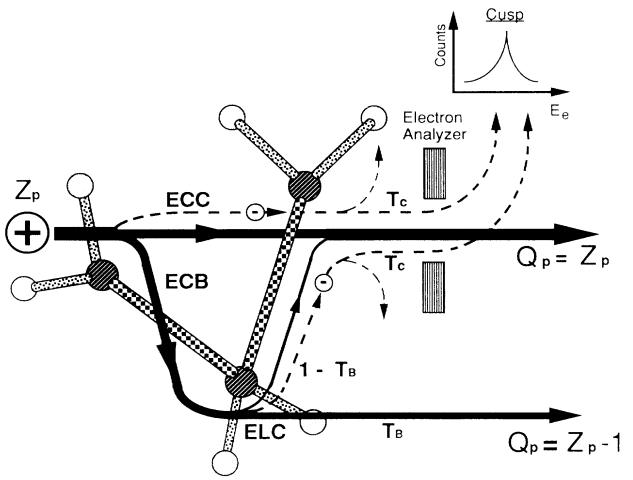

FIG. 1. The IMGO model schema for primary ECB or ECC in a hydrocarbon molecule followed by intramolecular secondary ELC or electron scattering processes (projectile charge states, ——; continuum electrons, ---Θ---).

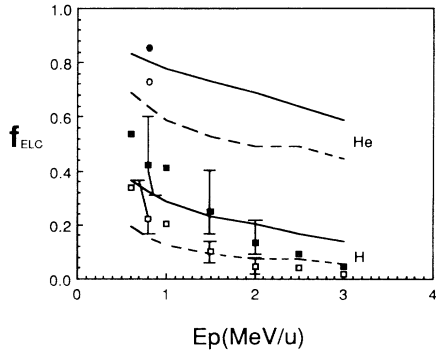

FIG. 2. f_{ELC} vs projectile energy for H^+ (squares) and He^{++} (circles) on CH_4 (open) and C_4H_8 (filled). Experimental values from Eq. (1) (H^+ σ_{ECB} data from [9], data estimated at 0.6, 1.0, and 2.5 MeV; He^{++} σ_{ECB} estimated from He^+ data [9]; σ_{ECC} estimated at 3 MeV—errors shown only on points with measured σ_{ECB} and σ_{ECC}). IMGO model generalization [Eq. (2)] for CH_4 (dashed line) and C_4H_8 (solid line) for H^+ (lower) and He^{++} (upper).

comprehensive way.

Following Fig. 1 it is straightforward to compute the fraction of ELC in the experimental ETC cusp obtained with a C_mH_n target as $f_{ELC}(C_mH_n)=\sigma_{ELC}(C_mH_n)T_c/[\sigma_{ECC}(C_mH_n)T_c+\sigma_{ELC}(C_mH_n)T_c]$, with the tacit assumption $T_c(\mathrm{ELC})=T_c(\mathrm{ECC})$. Dropping the parenthetical C_mH_n for conciseness, we can write

$$f_{ELC}=\{1+\sigma_{ECC}/[\sigma_{ECB}(1-T_B)]\}^{-1}. \quad (1)$$

Equation (1) exposes an underlying linkage in ETC between capture to bound and continuum states for small molecular targets which is also implicit in the discussion of cusp shapes for solid targets where multiple secondary collisions are significant—however, only for small molecular targets can the linkage be written so transparently.

For the initial calculations, we assume that the ELC contribution to the cusp is small, then $\sigma_{ETC}\cong\sigma_{ECC}$. Experimental "$\sigma_{ECC}$" values were derived for hydrocarbons from earlier cusp data [8], by normalizing to the CH_4 C K Auger electrons collected in the 0.6 MeV $H^+ + C_mH_n$ cusp electron spectra series [12]. Estimated errors in σ_{ECC} are $\sim\pm 50\%$. Experimental σ_{ECB} measurements ($\pm 6\%$) were taken directly from Ref. [7]. In Fig. 2 experimental f_{ELC} values for hydrocarbon targets of CH_4 and C_4H_8 have been computed from Eq. (1) for 0.6–3.0 MeV/nucleon H^+ and 0.8 MeV/nucleon He^{++} projectiles. Three major conclusions can be drawn from Fig. 2: (1) ELC contributes more to the He^{++} than the H^+ ETC cusp; (2) ELC contributes more to the C_4H_8 than the CH_4 ETC cusp; and (3) the ELC contribution to the ETC cusp decreases with increasing projectile energy. Figure 2 also indicates that ELC can be significant even for the smallest hydrocarbon molecule CH_4 in our projectile velocity range.

In the context of the IMGO model Eq. (1) can be generalized by using theoretical ratios for the bound-continuum cross sections. A particularly simple form for this ratio in our velocity range is available from the work of Lapicki and Losonsky if the ECB cross section is primarily $K\rightarrow K$ capture as in our case, viz., $\sigma_{ECB}(K)/\sigma_{ECC}\cong 2Z_p^3$, constant within $\sim 5\%$ over our velocity range [13]. Equation (1) then becomes

$$f_{ELC}\cong\{1+[2Z_p^3(1-T_B)]^{-1}\}^{-1}. \quad (2)$$

The "theoretical" predictions of Eq. (2) are shown in Fig. 2 for H and He projectiles. Agreement between experimental and predicted magnitudes and trends of f_{ELC} is good.

Earlier, $d\sigma/dE$ CH_4 cusps obtained with ~ 1 MeV/nucleon H^+ and He^{++} were considered "pure" ECC and subtracted from $m\geq 2$ hydrocarbon cusps to produce a difference spectrum, which had a statistically significant residue only for $m\geq 4$ [14]. The ratio of He to H residue peak yields displayed a "nominal" (meaning forced Z_p^x power-law fit) $Z_p^{2.8^{+0.6}_{-0.8}}$ dependence (2 standard deviation error) for 0.6 and 0.8 MeV/nucleon H^+ and He^{++} data [15]. An IMGO model calculation of the ELC dependence on the projectile charge comes from Eq. (2) by calculating the yield ratio using $Y_{ELC}\sim f_{ELC}\sigma_{ETC}$ for He and H. Our prior experimental results for ETC gave $\sigma_{ETC}\sim Z_p^2$ [15]. Numerical evaluation of the He/H f_{ELC} ratio at 0.8 MeV/nucleon produces a nominal $Z_p^{1.3}$ dependence; hence the product gives an overall nominal $Z_p^{3.3}$ dependence. Considering the inherent errors in both values this must be considered good agreement.

Alternative, supplemental evidence of ELC contributions to the cusp is exhibited by new $d^2\sigma/dE\,d\Omega$ (DDCS) spectra covering a 0° to $\sim 3°$ range, collected for 0.8 MeV/nucleon H^+ and He^{++} on CH_4 and C_4H_8 (He^{++} data shown in Fig. 3), obtained with the same spherical

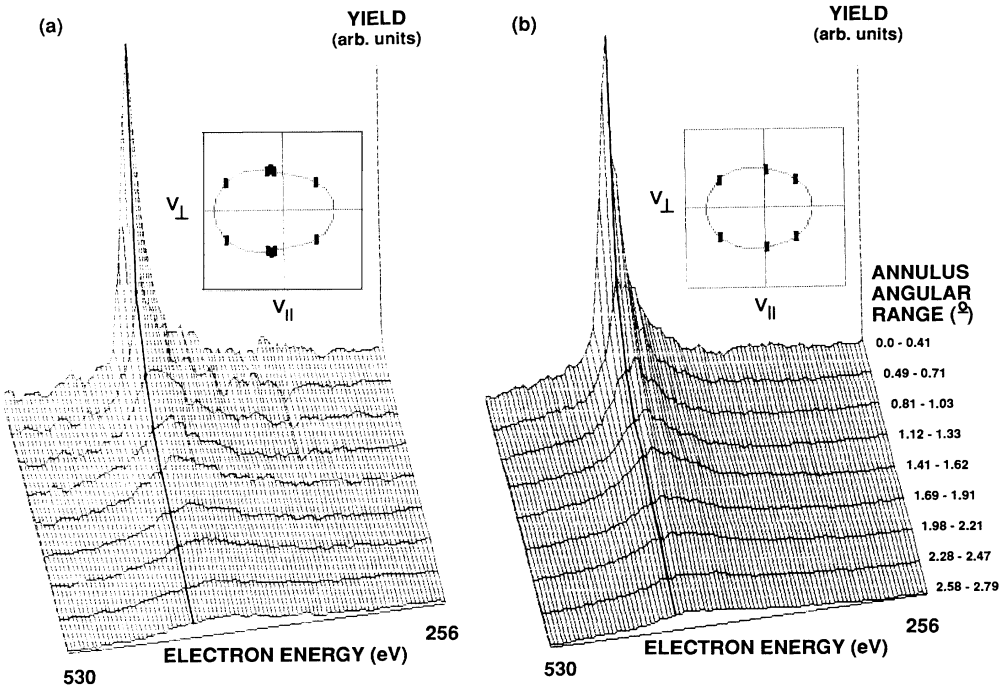

FIG. 3. Experimental $d^2\sigma/dE\,d\Omega$ cusp shape (normalized) for 0.8 MeV/nucleon He^{++} on (a) CH_4 and (b) C_4H_8. The constant-energy bold line drawn from the peak channel of the smallest annulus emphasizes peak shifts across the angular range. Inset: A contour slice through cusp at 0.4 of maximum in the projectile velocity frame (solid square, data; curve, Legendre polynomial fit).

sector electron analyzer employed in the $d\sigma/dE$ measurements [16,17]. The effective angular resolution of $\sim 0.3°$ was determined primarily by the exit aperture of the analyzer, and the angular distribution was centered within $\pm 0.2°$. Both experimental [17] and theoretical [18,19] work indicate that the peak of the DDCS ECC cusp exhibits a considerably larger droop toward lower energies with increasing detection angle than the ELC. Over the angular range shown in Fig. 3, the droop toward lower peak energies characteristic of ECC at larger angles is easily seen in the CH_4 spectrum, while the C_4H_8 cusp peak lies close to that for the smallest angle annulus, as expected for ELC.

The IMGO model analysis of the experimental DDCS, transformed to the projectile (prime) frame $\mathbf{v}_e' = \mathbf{v}_e = \mathbf{v}_p$) as shown in Fig. 3 (inset), evolves naturally from our prior discussion. In the projectile frame the standard representational form for ECC or ELC, viz., $d^2\sigma/d\mathbf{v}' = \sigma_0[\sum_k \beta_k P_k(\cos\theta')]/v_e'$, where β_k are the theoretical anisotropy coefficients (also called binary collision multipole moments), $\beta_0 = 1$, and σ_0 is the isotropic cross section, has *dominant* coefficients for ECC of β_0 and β_1 ($\beta_1 < 0$, $\beta_2 \simeq 0$), and β_0 and β_2 ($\beta_1 \cong 0$) for ELC [18]. The ETC DDCS is written as $d^2\sigma/d\mathbf{v}'|_{\rm ETC} = d^2\sigma/d\mathbf{v}'|_{\rm ECC} + d^2\sigma/d\mathbf{v}'|_{\rm ELC}$, or in the representational form

$$\left.\frac{d^2\sigma}{d\mathbf{v}'}\right|_{\rm ETC} \cong \frac{\sigma_0({\rm ECC})}{v_e'}\{1+\beta_1 P_1(\cos\theta') + w[1+\beta_2 P_2(\cos\theta')]\}\,, \qquad (3)$$

where the relative weight for the ELC term $w = \sigma_0({\rm ELC})/\sigma_0({\rm ECC})$. When the isotropic term in Eq. (3) is normalized to 1, it is seen that $w/(1+w) = f_{\rm ELC}$. These coefficients, when equated to those from a normalized Legendre polynomial fit of the form $1 + a_1 \times P_1(\cos\theta') + a_2 P_2(\cos\theta')$ to experimental contour slices with three to seven independent points (presented in Table I), provide the essential means to decompose the ETC contour into ELC and ECC contributions, giving $a_1 \simeq (1 - f_{\rm ELC})\beta_1$ and $a_2 \simeq f_{\rm ELC}\beta_2$. In this analysis, the

TABLE I. Coefficients from normalized Legendre polynomial fits to the projectile frame DDCS for 0.8 MeV/nucleon H^+ and He^{++} on CH_4 and C_4H_8. (Errors derived from uncertainty in cusp peak position.)

	Target			
	CH_4		C_4H_8	
Projectile	a_1	a_2	a_1	a_2
H^+	-0.53 ± 0.1	-0.17 ± 0.1	-0.49 ± 0.1	-0.02 ± 0.1
He^{++}	-0.20 ± 0.05	0.32 ± 0.05	-0.13 ± 0.05	0.20 ± 0.05

trends in the experimental a_1 and a_2 coefficients are as important as their magnitudes—in particular, note that a_1 decreases with increasing molecular size, and increasing Z_p, precisely as expected from f_{ELC} trends in Fig. 2 [20].

For bare projectiles in our velocity range ECC is essentially only from the C atoms, all of which are assumed to be equivalent, i.e., "atomic," with equal β_1 values, hence we can most reliably extract f_{ELC} by equating the coefficients of P_1. We extracted f_{ELC} by computing the ratio $a_1(H^+)/a_1(He^{++})$ for CH_4 and C_4H_8 from Table I, thereby eliminating the need to know β_1 but requiring its dependence on Z_p. By using Eq. (2), and assuming a Z_p exponent x ranging from $+1$ [5] to 0 and -1 [21] for the dependence of β_1, consistent with various theoretical predictions and experiment, we obtain values of f_{ELC} for (a) H^+ on CH_4 of 0.20, 0.16, and 0.07 ($x=+1,0,-1$), and on C_4H_8 of 0.37, 0.33, and 0.24, and (b) He^{++} on CH_4 of 0.85, 0.68, and 0.30, and on C_4H_8 of 0.92, 0.82, and 0.60. The $x=0,+1$ f_{ELC} values fall within error of the relevant total cross-section data points in Fig. 2, and display the observed Z_p and target size dependence. Conversely, if values of f_{ELC} were taken from Fig. 2, it would be possible to compute β_1 (or β_2) values from the fit data in Table I, and estimate their Z_p dependence.

The essentially independent approaches of cusp contour decomposition and total ECC and ECB cross-section ratios with relevant transmission fractions, both in the context of the IMGO model, are seen to lead to consistent f_{ELC} values. Since the IMGO model also leads naturally to a nominal Z_p^{-3} dependence for the ELC contribution to the $d\sigma/dE$ cusp in our velocity regime, consistent with experimental results, we believe the overall agreement provides substantial confirmation of the basic model applied here in analyzing electron transfer processes in small molecular targets.

We can conclude that the multiple charge-changing collisions encountered in molecules makes them inherently poor "stand-ins" for atoms in electron capture or loss experiments. For example, the IMGO model predicts $f_{ELC}\sim 0.18$ for 0.8 MeV/nucleon H^+ on a two-atom molecule such as O_2. By examining the trends in Fig. 2 we see where approximately atomic results, i.e., pure ECC, are obtainable, viz., for high-velocity, low-Z projectiles (unsurprising from purely qualitative considerations).

Another pertinent conclusion arises from the fact that the two-step ECB and ELC zero-degree electron cusp contribution is inseparable from the ECC cusp shape with nonatomic targets, using such straightforward experimental techniques as coincidences with exit charge state or target atom radiation. A "standard" ECC shape for a bare projectile incident on a nonatomic target does not exist; there is always a substantial, and variable, ELC component intermixed—a conclusion inherently consistent with observations of cusp ("convoy") yields [22] or multipole moment evolution [23] for varying thickness C foil targets.

By extending the purview of the IMGO model from its original explicit application in ECB from small molecules to the implicit ELC emerging from the secondary collision and its subsequent mingling with ECC, the magnitude and trends of all secondary intramolecular processes affecting ECB and ECC can now be accounted for in a consistent way. The bound-continuum linkage exposed here for small molecular targets can be formally displayed in the theoretical $2Z_p^3$ precept which couples capture to bound and continuum states when electron transfer is viewed via the IMGO model precept.

---

[a]Present address: Department of Physics, University of Central Arkansas, Conway, AR 72032.

[1] M. Breinig *et al.*, Phys. Rev. A **25**, 3015 (1982).
[2] W. Meckbach *et al.*, Phys. Rev. Lett. **57**, 1587 (1986).
[3] S. Suarez, W. Meckbach, G. C. Bernardi, and P. Focke, Z. Phys. D **7**, 309 (1988).
[4] G. Bissinger, J. M. Joyce, and R. Mehta, Nucl. Instrum. Methods Phys. Res., Sect. B **40/41**, 33 (1989).
[5] D. Jakubassa-Amundsen, Phys. Rev. A **38**, 70 (1988).
[6] Y. Yamazaki, L. H. Andersen, and H. Knudsen, J. Phys. B **23**, L317 (1990).
[7] G. Bissinger, J. M. Joyce, G. Lapicki, R. Laubert, and S. L. Varghese, Phys. Rev. Lett. **49**, 318 (1982).
[8] J. Gaiser, J. M. Joyce, and G. Bissinger, Phys. Rev. A **34**, 127 (1986).
[9] S. L. Varghese, G. Bissinger, J. M. Joyce, and R. Laubert, Phys. Rev. A **31**, 2202 (1985).
[10] T_B values agree quite well with, and are directly allied to, standard capture-loss equation calculations applied to a molecule as a superthin solid target (cf. Ref. [7]).
[11] σ_{ECB}, σ_{ECC}, and σ_{ELC} are all extremely forward directed, hence total cross sections are used.
[12] Using this normalization ~ 1 MeV/nucleon He^+ on Ar gives $\sigma_{ELC}\cong\sigma_{12}$ [stripping cross section for ~ 1 MeV/nucleon He^+ on Ar from R. C. Dehmel, H. K. Chau, and H. H. Fleischmann, At. Data **5**, 231 (1973)] as expected. G. Bissinger (to be published).
[13] G. Lapicki and W. Losonsky, Phys. Rev. A **15**, 896 (1977).
[14] G. Bissinger, J. Gaiser, J. M. Joyce, and M. Numan, Phys. Rev. Lett. **55**, 197 (1985).
[15] G. Bissinger, Nucl. Instrum. Methods Phys. Res., Sect. B **10/11**, 271 (1985), cf. Fig. 5 for 0.6 MeV/nucleon data.
[16] G. Bissinger and R. Mehta, Nucl. Instrum. Methods Phys. Res., Sect. B **56/57**, 92 (1991).
[17] S. B. Elston *et al.*, Phys. Rev. Lett. **55**, 2281 (1985).
[18] J. Burgdorfer, Phys. Rev. A **33**, 1578 (1986).
[19] J. Burgdorfer, M. Breinig, S. B. Elston, and I. A. Sellin, Phys. Rev. A **28**, 3277 (1983).
[20] Fits to our 0.6 MeV/nucleon H^+ and He^{++} on CH_4, C_3H_6, and C_7H_{16} ETC SDCS (Ref. [14]) by Y. Yu and G. Lapicki [Phys. Rev. A **36**, 4710 (1987)] agree with our molecular size a_1 and a_2 trends, but disagree with the projectile trends.
[21] Burgdorfer (Ref. [18]); (private communication).
[22] M. Hasegawa *et al.*, Phys. Lett. A **144**, 357 (1990).
[23] J. P. Gibbons *et al.*, Phys. Rev. Lett. **67**, 481 (1991).

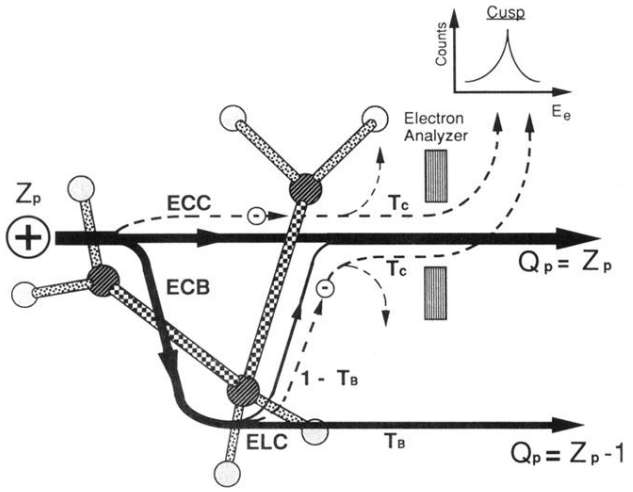

FIG. 1. The IMGO model schema for primary ECB or ECC in a hydrocarbon molecule followed by intramolecular secondary ELC or electron scattering processes (projectile charge states, ——; continuum electrons, ---⊖---).